Dynamical properties of magnetic topological insulator TBi_2Te_4 (T = Mn, Fe): phonons dispersion, Raman active modes, and chiral phonons study

Aksel Kobiałka,^{1,*} Małgorzata Sternik,^{2,†} and Andrzej Ptok^{2,‡}

¹Institute of Physics, Maria Curie-Skłodowska University, Plac Marii Skłodowskiej-Curie 1, PL-20031 Lublin, Poland ²Institute of Nuclear Physics, Polish Academy of Sciences, W. E. Radzikowskiego 152, PL-31342 Kraków, Poland (Dated: March 8, 2022)

Recently discovered magnetic topological insulators $T\text{Bi}_2\text{Te}_4$ (T=Mn, Fe) crystallize into the $R\bar{3}m$ rhombohedral structure and exhibit the antiferromagnetic order. Here, we discuss the lattice dynamics of these compounds to confirm the stability of these systems. We show that the phonon dispersion does not contain soft modes, so both compounds are dynamically stable in the $R\bar{3}m$ phase. We perform theoretical analyses of the mode activity at Γ point for the discussed compounds. In the case of the Raman active modes, our results are in agreement with the experimentally observed frequencies. Finally, we also discuss the possibility of realization of chiral phonons.

I. INTRODUCTION

 ${\rm MnBi_2Te_4}$ is the first intrinsic antiferromagnetic (AFM) topological insulator [1, 2] that has been recently observed experimentally. Similarly to the other topological insulators (TI), this system possesses a layered structure (Fig. 1), while layers are bonded by the van der Waals interaction. The AFM order exist below $T_{\rm N}=25~{\rm K}~[3-5],$ and is formed within Mn sublayers. Additionally, an interplay between the topological properties of this system and the intrinsic magnetic order allows for the realization of many quantum phenomena including quantum anomalous Hall effect [6, 7] or axion insulator state [8].

The topological properties of the MnBi₂Te₄ are exhibited by the realization of the electronic surface states [9–14], which in similarity to the case of TI (Bi₂Se₃ or Bi₂Te₃) form Dirac cones. However, contrary to the ordinary TI, due to the intrinsic magnetic order, the time reversal symmetry breaking occurs and the Dirac gap is observed in the surface states [15–17]. Nevertheless, these surface states can give a dominant contribution to the electron–phonon interaction [18–20].

More recently, a successful single crystal growth of FeBi₂Te₄ was reported [21]. The structure of this compound and its physical characteristics are not yet confirmed in a theoretical study, but it seems to have topological properties similar to the MnBi₂Te₄. In this paper, we present the theoretical study of the structure and lattice dynamics performed for both compounds, MnBi₂Te₄ and FeBi₂Te₄. We confirm the dynamical stability of both crystals and the consistency between calculated and measured data on both structural parameters and their Raman shifts. Moreover, we calculate the circular polarization of Te and Bi atoms and demonstrate that the

The paper is organized as follows. First, we briefly describe the computational details (Sec. II). The phonon dispersions are presented and discussed in Sec. III. Next, in Sec. IV, we discuss thoroughly the Raman active modes in relation to the available experimental and theoretical results. In Sec. V, we discuss the realization of the chiral phonons in the $T\mathrm{Bi}_2\mathrm{Te}_4$. Finally, we conclude our findings in Sec. VI.

II. CALCULATION DETAILS

The first-principles (DFT) calculations were performed using the projector augmented-wave (PAW) potentials [22] implemented in the Vienna Ab initio Simulation Package (VASP) code [23–25]. The calculations are made within the generalized gradient approximation (GGA) in the Perdew, Burke, and Ernzerhof (PBE) parametrization [26]. Strong local electron interaction on the 3d orbitals of transition metals were taken into account using DFT+U scheme [27], with the intraorbital Coulomb parameter U=5.0 eV, similarly to the earlier studies [28]. Additionally, we included the spin–orbit coupling (SOC) as well as the van der Waals (vdW) cor-

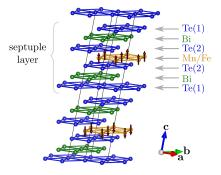


FIG. 1. Magnetic unit cell of antiferromagnetic topological insulator $T\mathrm{Bi_2Te_4}$ ($T=\mathrm{Mn,\ Fe}$).

emergence of chiral modes in these materials is feasible.

^{*} e-mail: akob@kft.umcs.lublin.pl

[†] e-mail: sternik@wolf.ifj.edu.pl

[‡] e-mail: aptok@mmj.pl

rections within the Grimme scheme (DFT-D2) [29].

The magnetic unit cells were optimized using $24 \times 24 \times 4$ k-point Γ -centered grids in the Monkhorst-Pack scheme [30]. The energy cutoff for the plane-wave expansion is set to 450 eV. The condition for the breaking of the optimization loop was the energy difference of 10^{-6} eV and 10^{-8} eV for ionic and electronic degrees of freedom for subsequent steps. The crystal symmetry was analysed using FINDSYM [31] and SPGLIB [32], while the momentum space analysis was done using SEEK-PATH tools [33].

The dynamical properties were calculated using the direct Parlinski-Li-Kawazoe method [34]. Under this calculation, the interatomic force constants (IFC) are found from the forces acting on atoms when an individual atom is displaced. The forces were obtained by the first-principle calculations with VASP using the supercell containing $3 \times 3 \times 1$ magnetic unit cells and reduced Γ -centered $3 \times 3 \times 2$ k mesh. The phonon dispersion and polarization vectors analyses were performed using the Alamode software [35]. The mode symmetries at the Γ point were found by the Phonon software [36].

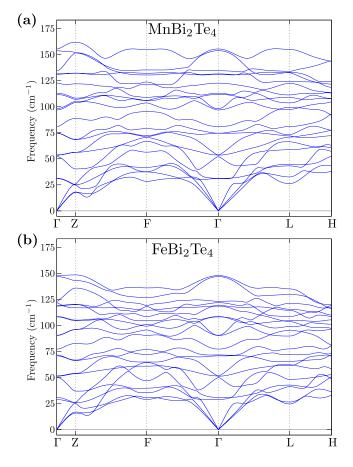


FIG. 2. The phonon dispersion along high symmetry points.

III. LATTICE DYNAMICS

Crystal structure. — TBi₂Te₄ crystallizes in the $R\bar{3}m$ (space group 166) rhombohedral structure presented in Fig. 1. This system is composed of septuple layer (SL) slabs (containing the sequence of Te(1)-Bi-Te(2)-(Mn/Fe)-Te(2)-Bi-Te(1) atoms), separated by the vdW gap between Te(1) double-layer. After the optimization, we obtain the lattice constants a = 4.29 Å, and c = 41.67 Å for MnBi₂Te₄, and a = 4.26 Å, and c = 41.46 Å for FeBi₂Te₄. Our theoretical findings are in the excellent agreement with experimental results, i.e., $a = 4.33 \text{ Å}, \text{ and } c = 40.92 \text{ Å for MnBi}_2\text{Te}_4 [37] \text{ and}$ a = 4.39 Å, and c = 42.69 Å for FeBi₂Te₄ [21]. Atoms are located in Wyckoff position 6c $(0,0,z_{Bi})$, 6c $(0,0,z_{Te(1)})$, $6c (0,0,z_{Te(2)})$, and 3c (0,0,0), for Bi, Te(1), Te(2), and T=Mn, Fe atoms, respectively. We find $z_{Bi}=0.42$, $z_{\mathrm{Te}(1)}=0.13,$ and $z_{\mathrm{Te}(2)}=0.29$ for both compounds.

Phonon dispersion. — The phonon dispersions of TBi_2Se_4 are presented in Fig. 2. Introduction of the spinorbit interaction in the calculations does not change the phonon dispersion qualitatively. In the phonon dispersion, all acoustic branches show a linear dispersion in the vicinity of the Γ point. No imaginary phonon frequency was found for any system, which indicates the stability of these systems in the $R\bar{3}m$ phase. For this reason, we can expect that the small substitution of Fe should be possible for the base system MnBi₂Se₄, contrary to the hole doping by Ca or Mg, which leads to substantial instability in the recently studied systems [38].

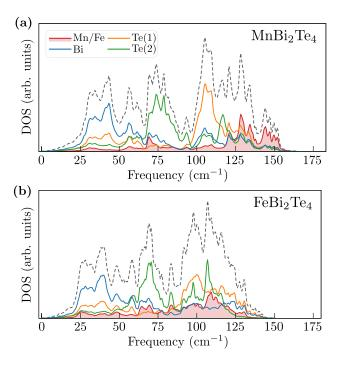


FIG. 3. The total (dashed line) and partial (solid lines) phonon density of states.

TABLE I. Characteristic frequencies in cm⁻¹, activities (R - Raman, IR - infrared) and symmetries of the modes at Γ point.

	${ m MnBi_2Te_4}$			$\mathrm{FeBi}_{2}\mathrm{Te}_{4}$	
freq.	activity	symm.	freq.	activity	symm.
30.65	R	$E_{\rm g}$	29.35	R	E_{g}
51.20	R	$A_{1\mathrm{g}}$	49.17	\mathbf{R}	$A_{1\mathrm{g}}$
52.67	IR	E_{u}	50.60	$_{ m IR}$	E_{u}
73.32	\mathbf{R}	E_{g}	70.05	R	$E_{ m g}$
76.66	IR	$A_{2\mathrm{u}}$	76.02	$_{ m IR}$	$A_{2\mathrm{u}}$
95.90	IR	E_{u}	88.93	$_{ m IR}$	$E_{ m u}$
110.51	R	$E_{\rm g}$	106.57	\mathbf{R}	$E_{ m g}$
120.58	R	$A_{1\mathrm{g}}$	116.92	$_{ m IR}$	$E_{ m u}$
129.16	IR	E_{u}	119.82	\mathbf{R}	$A_{1\mathrm{g}}$
132.23	IR	$A_{2\mathrm{u}}$	121.05	$_{ m IR}$	$A_{2\mathrm{u}}$
151.21	\mathbf{R}	$A_{1\mathrm{g}}$	144.23	$_{ m IR}$	$A_{2\mathrm{u}}$
152.84	IR	$A_{2\mathrm{u}}$	145.37	\mathbf{R}	$A_{1\mathrm{g}}$

Phonon density of states. — The total and partial density of states are presented in Fig. 3. As we can see, the vibrational modes of heavy Bi contribute mainly to the low range of frequencies. Vibrations of Te in the first and second position [i.e. Te(1) and Te(2)], are placed in two separated frequency areas at the middle frequency region between T = (Mn,Fe) and Bi atomic layers. The Te(1) atoms, which create a two-layer-like structure (see Fig. 1), vibrate with higher frequencies (around 100 cm⁻¹) than the Te(2) atoms that oscillate with average frequency of 75 cm⁻¹. Finally, T = (Mn, Fe) modes are located in the range of high frequencies. Interestingly, for both systems, the phonon dispersion associated with these modes creates a flat band around 130 cm⁻¹ or 120 cm⁻¹ in Mn or Fe compounds, respectively (see Fig. 2).

RAMAN ACTIVE MODES

Irreducible representations. — The phonon modes of TBi_2Te_4 at Γ point can be decomposed into the irreducible representations of the space group $R\bar{3}m$ as follows:

$$\begin{split} \Gamma_{\rm acoustic} &= A_{\rm 2u} + E_{\rm u}, \\ \Gamma_{\rm optic} &= 3A_{\rm 1g} + 3A_{\rm 2u} + 3E_{\rm u} + 3E_{\rm g}. \end{split}$$

In total, there are 21 vibrational modes, seven nondegenerate A_{1g} and A_{2u} modes, and seven doubly degenerate $E_{\rm u}$ and $E_{\rm g}$ modes. Here, optical vibrations $3A_{\rm 2u}+3E_{\rm u}$ are infrared active (IR), while optical modes $3A_{1g} + 3E_{g}$ are Raman (R) active. The activity and symmetries of the modes at Γ point for TBi_2Te_4 are presented in Tab I.

The atoms participating in the vibrations of the $E_{\rm g}$ and $E_{\rm u}$ types oscillate in the SL plane (a-b plane in Fig. 1). Contrary to this, the modes A_{1g} and A_{2u} are related

TABLE II. Selection rules for Raman-active modes.

configuration	A_{1g}	$E_{ m g}$
e_x in e_x out (linear \parallel)	$ a ^2$	$ c ^2$
e_x in e_y out (linear \perp)	0	$ c ^2$
σ^+ in σ^+ out (cocircular)	$2 a ^{2}$	0
σ^+ in σ^- out (cross-circular)	0	$2 c ^2$

to out-of-plane oscillations (perpendicular to a-b plane). Interestingly, the magnetic T atoms do not participate in the vibrations of the Raman active modes (i.e. A_{1g} and

Selection rules for Raman-active modes. — The nonresonant Raman scattering intensity depends in general on the directions of the incident and scattered light relative to the principal axes of the crystal. It is expressed by Raman tensor R, relevant for a given crystal symmetry, as [39]:

$$I \propto |e_i \cdot R \cdot e_s|^2,\tag{1}$$

where e_i and e_s are the polarization vectors of the incident and scattered light. respectively. According to the group theory, the Raman tensor for the $R\bar{3}m$ space group takes the following forms for the A_{1g} and E_{g} modes:

$$R(A_{1g}) = \begin{pmatrix} a & 0 & 0 \\ 0 & a & 0 \\ 0 & 0 & b \end{pmatrix} \quad \text{and}$$
 (2)

$$R(A_{1g}) = \begin{pmatrix} a & 0 & 0 \\ 0 & a & 0 \\ 0 & 0 & b \end{pmatrix} \text{ and } (2)$$

$$R(E_{g}^{I}) = \begin{pmatrix} c & 0 & 0 \\ 0 & -c & d \\ 0 & d & 0 \end{pmatrix}; R(E_{g}^{II}) = \begin{pmatrix} 0 & -c & -d \\ -c & 0 & 0 \\ -d & 0 & 0 \end{pmatrix}.$$

In the backscattering configuration, e_i and e_s are placed within the xy plane. The polarization vectors for linearly polarized light in the x and y directions are $e_x = (1 \ 0 \ 0)$ and $e_y = (0 \ 1 \ 0)$, respectively. Similarly, the polarization vector for left σ^+ and right σ^- circularly polarized light are $\sigma^{\pm}=\frac{1}{\sqrt{2}}(1\pm i\,0)$. Using Eq. (1) and the Raman tensors (2), we can determine the selection rules and Raman intensities for various scattering geometries. Tab. II summarized the Raman response in the backscattering geometry for four polarization configurations. As we can see, it is possible to distinguish the A_{1g} and E_{g} using the different backscattering configurations. The same holds for both linear and circularly polarized Raman spectra measurements. For example, this property of the Raman modes was used to differentiate between Raman active modes using co- and cross-circular Raman back-scattering in Ref. [40]. The group theory study of the vibrational modes in bulk paramagnetic TBi₂Te₄, the phonon selection rules, and the real-space displacements corresponding to each mode are presented in Ref. [41].

Comparison with related results. — In Tab. III, we present a comparison of our theoretically obtained frequencies of the Raman active modes with previous results (both experimental and theoretical). It should be

TABLE III. Comparison of the Raman active modes frequencies (cm⁻¹) for different compounds.

$E_{\rm g}$	A_{1g}	$E_{\rm g}$	$E_{\rm g}$	$A_{1\mathrm{g}}$	A_{1g}					
$\mathbf{MnBi}_{2}\mathbf{Te}_{4}$										
30.65	51.20	73.32	110.51	120.58	151.21	this work				
_	46	65	102		138	${\it measurement}$	[37]			
_	47.4	67.4	104.2	_	139.8	${\it measurement}$	[42]			
_	45.7	66.9	103.4	113.5	138.6	${\it measurement}$	[40]			
26.9	48.0	68.3	105.1	115.6	140.0	${\it measurement}$	[45]			
_	47	60	105	_	142	calculation	[37]			
30.3	46.0	74.5	109.6	117.4	144.1	calculation	[40]			
29.4	51.8	73.4	109.1	119.4	149.1	calculation	[45]			
$\phantom{aaaaaaaaaaaaaaaaaaaaaaaaaaaaaaaaaaa$										
29.35	49.17	70.05	106.57	119.82	145.37	this work				
	_	65		110	132	${\it measurement}$	[21]			
$\mathbf{Bi_2Te_3}$										
_	62.5	_	103	_	134	measurement	[46]			
_	61.5	_	101.5		133.5	${\it measurement}$	[47]			
_	62.3	_	103		134	${\it measurement}$	[48]			
34.4	62.1	_	101.7		134.0	measurement	[49]			
42.4	66.4	_	106.7		134.8	calculation	[50]			
42.1	64.2	_	112.3		139.2	calculation	[47]			
50.6	71.1	—	118.5	—	128.3	calculation	[51]			

mentioned that not all Raman modes can be observed at each measurement. This is caused by the relatively weak intensity of some Raman modes and the insensitivity of the used method for observing low-frequency modes. For example, for MnBi₂Te₄, in Ref. [37] or [42] only four Raman frequencies are observed, while in Ref. [40] we can distinguish five distinctive peaks. Similarly, in the case of the FeBi₂Te₄, the Raman spectroscopy experiment exhibits three distinct phonon modes at 65 cm⁻¹, 110 cm⁻¹, and 132 cm⁻¹ along with two split secondary modes at 90 cm^{-1} , and 144 cm^{-1} [21]. The measured frequencies are slightly lower than the values obtained in calculations. The biggest difference of $\sim 12~{\rm cm}^{-1}$ is observed for the high-frequency A_{1q} mode. The reason for that can be the temperature at which the measurement is carried out. Recent experiments on MnBi₂Te₄ show that the increase of temperature [40] leads to the shift of the Raman frequency modes to lower values. Similar temperature dependence of the Raman frequencies was observed for isostructural materials, PbBi₂Te₄ [43] and GeBi₂Te₄ [44]. In contrast, the external pressure imposed on the MnBi₂Te₄ crystal causes the increase of mode frequencies [42].

Finally, we briefly describe the differences between the Raman frequencies in $T\mathrm{Bi}_2\mathrm{Te}_4$ and in the parent $\mathrm{Bi}_2\mathrm{Te}_3$ material. In the studied materials, the $T\mathrm{Te}$ layer is inserted in van der Waals gaps of $\mathrm{Bi}_2\mathrm{Te}_3$ layers. Due to similar crystal structures described by the same space group symmetry, the four Raman modes of $\mathrm{Bi}_2\mathrm{Te}_3$ cor-

respond to four Raman modes of $T\mathrm{Bi}_2\mathrm{Te}_4$. The smaller number of Raman active modes is caused by the smaller number of atoms in the unit cell. The modifications of the crystal structure induced by additional $T\mathrm{Te}$ layers lead to the changes of distance and strength of the covalent bonds between pairs of atoms. This, in turn, results in the shift of Raman modes (cf. Tab. III).

For example, the frequency of the first $A_{1\rm g}$ mode is reduced from $\sim 62~{\rm cm^{-1}}$ in ${\rm Bi_2Se_3}$ to $\sim 50~{\rm cm^{-1}}$ in $T{\rm Bi_2Se_4}$, while the high-frequency $A_{1\rm g}$ is shifted from $\sim 135~{\rm cm^{-1}}$ for ${\rm Bi_2Te_3}$ to $\sim 140~{\rm cm^{-1}}$ for $T{\rm Bi_2Te_4}$. Contrary to this, the $E_{\rm g}$ modes are almost unchanged. As we mentioned previously, $A_{1\rm g}$ and $E_{\rm g}$ modes realize the out-of-plane and in-plane vibrations, respectively [41], and thus the distance between Te–Bi plays a crucial role [43]. Because the covalent interactions are much stronger along Te(1)–Bi–Te(2) than between Te–Te and Bi–Bi pairs, only the $A_{1\rm g}$ mode is shifted.

V. CIRCULAR PHONON POLARIZATION

The helicity of incident photons is completely reversed in the Raman process involving the double degenerated $E_{\rm g}$ modes. This phenomenon is highly relevant in the context of circularly polarized phonons [52–56]. Indeed, $T{\rm Bi}_2{\rm Te}_4$ possesses the C_{3v} symmetry (each layer of atoms inside the SL makes a triangular lattice), which allows for the realization of circularly polarized phonons [57]. Although none of modes at Γ point have the intrinsic chirality, we can obtain the chiral phonons via superimposing the doubly degenerate $E_{\rm g}$ modes [58]. Nevertheless, the chiral phonons can emerge out of the center of the Brillouina zone (i.e. away from the Γ point), where degeneracy is lifted.

The circular polarization of the phonons can be studied by analyzing the phonon polarization vector, which can be found from the diagonalization of the dynamical matrix:

$$D_{\alpha\beta}^{jj'}(\boldsymbol{q}) \equiv \frac{1}{\sqrt{m_j m_{j'}}} \sum_{n} \Phi_{\alpha\beta}(j0, j'n) \exp\left(i\boldsymbol{q} \cdot \boldsymbol{R}_{j'n}\right),$$
(3)

where q is the phonon wave vector and m_j denotes the mass of jth atom. Here $\Phi_{\alpha\beta}(j0,j'n)$ is the IFC tensor (α and β denotes the direction index, i.e. x, y, and z) between jth and j'th atoms located in the initial (0) and nth primitive unit cell. Then, the phonon spectrum as well as the polarization vectors are given by the eigenproblem of the dynamical matrix:

$$\omega_{\varepsilon \boldsymbol{q}}^{2} e_{\varepsilon \boldsymbol{q} \alpha j} = \sum_{j'\beta} D_{\alpha\beta}^{jj'}(\boldsymbol{q}) e_{\varepsilon \boldsymbol{q} \beta j'}. \tag{4}$$

Here, the ε branch describes the phonon with a frequency $\omega_{\varepsilon \boldsymbol{q}}$ and a polarization vector $\mathbf{e}_{\varepsilon \boldsymbol{q} \alpha j}$. Each αj component of the polarization vector is associated with the displacement of the jth atom in the α th direction.

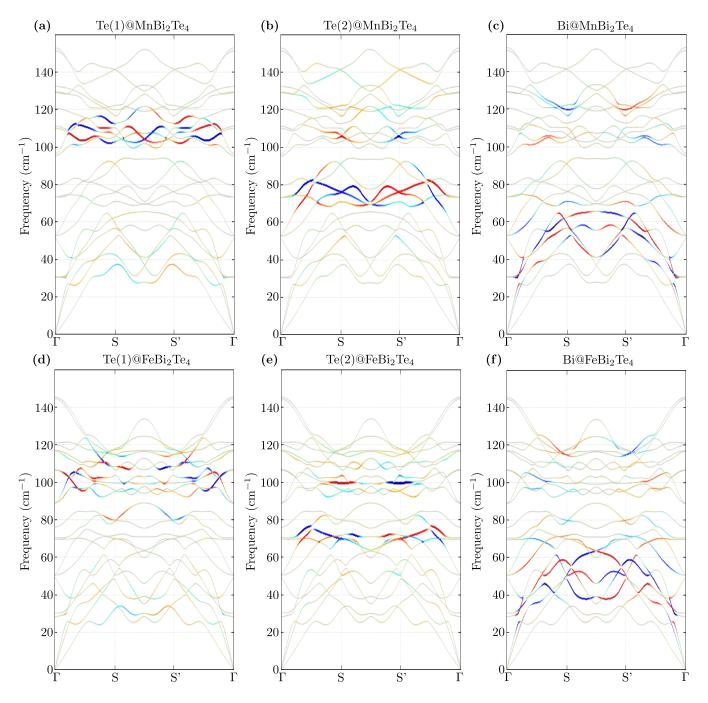


FIG. 4. Circular polarization of Te(1), Te(2), and Bi (panels from left to right) for MnBi₂Te₄ and FeBi₂Te₄ (top and bottom panels, respectively). Red and blue lines denotes left and right handed circular polarization of phonons, while the line width corresponds to the circulation value.

The phonon mode related to the particular polarization vector $\mathbf{e}_{\varepsilon \boldsymbol{q} \alpha j}$ can be discussed in the context of the circular polarization. For this purpose, we introduce a new basis defined as [54-56]: $|R_1\rangle \equiv \frac{1}{\sqrt{2}} \left(1 \ i \ 0 \cdots 0\right)^T;$ $|L_1\rangle \equiv \frac{1}{\sqrt{2}} \left(1 \ i \ 0 \cdots 0\right)^T;$ $|Z_1\rangle \equiv \frac{1}{\sqrt{2}} \left(0 \ 0 \ 1 \cdots 0\right)^T;$ $\cdots;$ $|R_j\rangle \equiv \frac{1}{\sqrt{2}} \left(\cdots 1 \ i \ 0 \cdots 0\right)^T;$ $|L_j\rangle \equiv \frac{1}{\sqrt{2}} \left(\cdots 1 \ -i \ 0 \cdots 0\right)^T;$ $|Z_j\rangle \equiv \frac{1}{\sqrt{2}} \left(\cdots 0 \ 0 \ 1 \cdots 0\right)^T;$ \cdots . It means that two in-

plane components are replaced by the circular polarization vectors σ^{\pm} (defined in Sec. IV), while the third component is unchanged. In this basis, each polarization vector, $e \equiv e_{\varepsilon} q_{\alpha j}$, is represented as:

$$e = \sum_{j} \left(\alpha_j^R | R_j \rangle + \alpha_j^L | L_j \rangle + \alpha_j^Z | Z_j \rangle \right), \qquad (5)$$

where $\alpha_j^V=\langle V_j|{\rm e}\rangle,$ for $V\in\{R,L,Z\}$ and $j\in\{1,2,\cdots,N\}$ (N is a total number of atoms in a prim-

itive unit cell). The way of the jth atom movement is determined by a circulation $\mathcal{C} = |\alpha_j^R|^2 - |\alpha_j^L|^2$. When $\mathcal{C} = 0$, the atom is involved in an ordinary non-circular vibration, and when $\mathcal{C} \neq 0$, it realizes a circular motion.

In $T\text{Bi}_2\text{Te}_4$, T atoms do not exhibit circular vibrations, being the only magnetic atoms in the compound. The other atoms, Te(1), Te(2), and Bi, realize a circular motion with different frequencies. Fig. 4 presents a circular polarization of Te(1), Te(2), and Bi, along a path between two Γ points in a-b plane (cf. Fig. 1). As the system possesses the inversion symmetry, atoms from opposite sites of the SL layer have an opposite circulation (i.e. the total circulation of the system is zero). The chiral phonons of Te(1), Te(2), and Bi are located around 110 cm⁻¹, 75 cm⁻¹, and 50 cm⁻¹. This "separation" of different types of phonons generating a circular motion of atoms is in agreement with the discussion of the phonon DOS (cf. Sec. III).

VI. SUMMARY

In this paper, we investigated the dynamical properties of $T\text{Bi}_2\text{Te}_4$ (T=Mn, Fe) compounds. Both systems crystallize in the $R\bar{3}m$ rhombohedral structure. The phonon dispersion relations do not exhibit any imaginary frequencies and thus, both compounds are dynamically

stable. We performed the analyses of the mode symmetries at the Γ point. The Raman and infrared active modes were calculated. The frequencies of the Raman active modes are in agreement with previous theoretical and experimental results. We point out that the Raman backscattering using co- or cross-circular configuration can be useful in distinguishing the A_{1g} and E_{g} Raman active mode. Additionally, we show that the initially double degenerate E_{g} modes (at the Γ point), give rise to emergence of the circularly polarized modes away from the Γ point. Moreover, chiral phonon modes are separated in the frequency domain depending on the atomic layer within the septuple layer.

ACKNOWLEDGMENTS

Some figures in this work were rendered using VESTA [59]. This work was supported by National Science Centre (NCN, Poland) under Projects No. 2018/31/N/ST3/01746 (A.K.), 2017/25/B/ST3/02586 (M.S.), and 2016/21/D/ST3/03385 (A.P.). In addition, A.P. appreciates funding in the frame of scholarship of the Minister of Science and Higher Education of Poland for outstanding young scientists (2019 edition, No. 818/STYP/14/2019).

- M. M. Otrokov, I. I. Klimovskikh, H. Bentmann, D. Estyunin, A. Zeugner, Z. S. Aliev, S. Gaß, A. U. B. Wolter, A. V. Koroleva, A. M. Shikin, M. Blanco-Rey, M. Hoffmann, I. P. Rusinov, A. Y. Vyazovskaya, S. V. Eremeev, Y. M. Koroteev, V. M. Kuznetsov, F. Freyse, J. Sánchez-Barriga, I. R. Amiraslanov, M. B. Babanly, N. T. Mamedov, N. A. Abdullayev, V. N. Zverev, A. Alfonsov, V. Kataev, B. Büchner, E. F. Schwier, S. Kumar, A. Kimura, L. Petaccia, G. Di Santo, R. C. Vidal, S. Schatz, K. Kißner, M. Ünzelmann, C. H. Min, S. Moser, T. R. F. Peixoto, F. Reinert, A. Ernst, P. M. Echenique, A. Isaeva, and E. V. Chulkov, Prediction and observation of an antiferromagnetic topological insulator, Nature 576, 416 (2019).
- [2] Y. Gong, J. Guo, J. Li, K. Zhu, M. Liao, X. Liu, Q. Zhang, L. Gu, L. Tang, X. Feng, D. Zhang, W. Li, C. Song, L. Wang, P. Yu, X. Chen, Y. Wang, H. Yao, W. Duan, Y. Xu, S.-C. Zhang, X. Ma, Q.-K. Xue, and K. He, Experimental realization of an intrinsic magnetic topological insulator, Chinese Phys. Lett. 36, 076801 (2019).
- [3] J.-Q. Yan, Q. Zhang, T. Heitmann, Z. Huang, K. Y. Chen, J.-G. Cheng, W. Wu, D. Vaknin, B. C. Sales, and R. J. McQueeney, Crystal growth and magnetic structure of mnbi₂te₄, Phys. Rev. Materials 3, 064202 (2019).
- [4] L. Ding, C. Hu, F. Ye, E. Feng, N. Ni, and H. Cao, Crystal and magnetic structures of magnetic topological insulators MnBi₂Te₄ and MnBi₄Te₇, Phys. Rev. B 101, 020412(R) (2020).

- [5] H. Li, S. Liu, C. Liu, J. Zhang, Y. Xu, R. Yu, Y. Wu, Y. Zhang, and S. Fan, Antiferromagnetic topological insulator MnBi₂Te₄: synthesis and magnetic properties, Phys. Chem. Chem. Phys. 22, 556 (2020).
- [6] Y. Deng, Y. Yu, M. Z. Shi, Z. Guo, Z. Xu, J. Wang, X. H. Chen, and Y. Zhang, Quantum anomalous hall effect in intrinsic magnetic topological insulator MnBi₂Te₄, Science 367, 895 (2020).
- [7] D. Ovchinnikov, X. Huang, Z. Lin, Z. Fei, J. Cai, T. Song, M. He, Q. Jiang, C. Wang, H. Li, Y. Wang, Y. Wu, D. Xiao, J.-H. Chu, J. Yan, C.-Z. Chang, Y.-T. Cui, and X. Xu, Intertwined topological and magnetic orders in atomically thin Chern insulator MnBi₂Te₄, Nano Lett. 21, 2544 (2021).
- [8] C. Liu, Y. Wang, H. Li, Y. Wu, Y. Li, J. Li, K. He, Y. Xu, J. Zhang, and Y. Wang, Robust axion insulator and Chern insulator phases in a two-dimensional antiferromagnetic topological insulator, Nat. Mater. 19, 522 (2020).
- [9] Y.-J. Hao, P. Liu, Y. Feng, X.-M. Ma, E. F. Schwier, M. Arita, S. Kumar, C. Hu, R. Lu, M. Zeng, Y. Wang, Z. Hao, H.-Y. Sun, K. Zhang, J. Mei, N. Ni, L. Wu, K. Shimada, C. Chen, Q. Liu, and C. Liu, Gapless surface Dirac cone in antiferromagnetic topological insulator MnBi₂Te₄, Phys. Rev. X 9, 041038 (2019).
- [10] B. Chen, F. Fei, D. Zhang, B. Zhang, W. Liu, S. Zhang, P. Wang, B. Wei, Y. Zhang, Z. Zuo, J. Guo, Q. Liu, Z. Wang, X. Wu, J. Zong, X. Xie, W. Chen, Z. Sun, S. Wang, Y. Zhang, M. Zhang, X. Wang, F. Song, H. Zhang, D. Shen, and B. Wang, Intrinsic magnetic

- topological insulator phases in the Sb doped MnBi₂Te₄ bulks and thin flakes, Nat. Commun. 10, 4469 (2019).
- [11] Y.-J. Hao, P. Liu, Y. Feng, X.-M. Ma, E. F. Schwier, M. Arita, S. Kumar, C. Hu, R. Lu, M. Zeng, Y. Wang, Z. Hao, H.-Y. Sun, K. Zhang, J. Mei, N. Ni, L. Wu, K. Shimada, C. Chen, Q. Liu, and C. Liu, Gapless surface Dirac cone in antiferromagnetic topological insulator MnBi₂Te₄, Phys. Rev. X 9, 041038 (2019).
- [12] Y. J. Chen, L. X. Xu, J. H. Li, Y. W. Li, H. Y. Wang, C. F. Zhang, H. Li, Y. Wu, A. J. Liang, C. Chen, S. W. Jung, C. Cacho, Y. H. Mao, S. Liu, M. X. Wang, Y. F. Guo, Y. Xu, Z. K. Liu, L. X. Yang, and Y. L. Chen, Topological electronic structure and its temperature evolution in antiferromagnetic topological insulator MnBi₂Te₄, Phys. Rev. X 9, 041040 (2019).
- [13] W. Ko, M. Kolmer, J. Yan, A. D. Pham, M. Fu, F. Lüpke, S. Okamoto, Z. Gai, P. Ganesh, and A.-P. Li, Realizing gapped surface states in the magnetic topological insulator MnBi_{2-x}Sb_xTe₄, Phys. Rev. B **102**, 115402 (2020).
- [14] D. Nevola, H. X. Li, J.-Q. Yan, R. G. Moore, H.-N. Lee, H. Miao, and P. D. Johnson, Coexistence of surface ferromagnetism and a gapless topological state in MnBi₂Te₄, Phys. Rev. Lett. **125**, 117205 (2020).
- [15] A. M. Shikin, D. A. Estyunin, I. I. Klimovskikh, S. O. Filnov, E. F. Schwier, S. Kumar, K. Miyamoto, T. Okuda, A. Kimura, K. Kuroda, K. Yaji, S. Shin, Y. Takeda, Y. Saitoh, Z. S. Aliev, N. T. Mamedov, I. R. Amiraslanov, M. B. Babanly, M. M. Otrokov, S. V. Eremeev, and E. V. Chulkov, Nature of the Dirac gap modulation and surface magnetic interaction in axion antiferromagnetic topological insulator MnBi₂Te₄, Sci. Rep. 10, 13226 (2020).
- [16] A. M. Shikin, D. A. Estyunin, N. L. Zaitsev, D. Glazkova, I. I. Klimovskikh, S. O. Filnov, A. G. Rybkin, E. F. Schwier, S. Kumar, A. Kimura, N. Mamedov, Z. Aliev, M. B. Babanly, K. Kokh, O. E. Tereshchenko, M. M. Otrokov, E. V. Chulkov, K. A. Zvezdin, and A. K. Zvezdin, Sample-dependent dirac-point gap in MnBi₂Te₄ and its response to applied surface charge: A combined photoemission and ab initio study, Phys. Rev. B 104, 115168 (2021).
- [17] X.-M. Ma, Y. Zhao, K. Zhang, S. Kumar, R. Lu, J. Li, Q. Yao, J. Shao, F. Hou, X. Wu, M. Zeng, Y.-J. Hao, Z. Hao, Y. Wang, X.-R. Liu, H. Shen, H. Sun, J. Mei, K. Miyamoto, T. Okuda, M. Arita, E. F. Schwier, K. Shimada, K. Deng, C. Liu, J. Lin, Y. Zhao, C. Chen, Q. Liu, and C. Liu, Realization of a tunable surface Dirac gap in Sb-doped MnBi₂Te₄, Phys. Rev. B 103, L121112 (2021).
- [18] J. A. Sobota, S.-L. Yang, D. Leuenberger, A. F. Kemper, J. G. Analytis, I. R. Fisher, P. S. Kirchmann, T. P. Devereaux, and Z.-X. Shen, Distinguishing bulk and surface electron-phonon coupling in the topological insulator Bi₂Se₃ using time-resolved photoemission spectroscopy, Phys. Rev. Lett. 113, 157401 (2014).
- [19] R. Heid, I. Y. Sklyadneva, and E. V. Chulkov, Electronphonon coupling in topological surface states: The role of polar optical modes, Sci. Rep. 7, 1095 (2017).
- [20] G. Benedek, S. Miret-Artés, J. R. Manson, A. Ruck-hofer, E. Ernst, W, and A. Tamtögl, Origin of the electron-phonon interaction of topological semimetal surfaces measured with helium atom scattering, J. Phys. Chem. Lett. 11, 1927 (2020).
- [21] A. Saxena, P. Rani, V. Nagpal, S. Patnaik, I. Felner, and V. P. S. Awana, Crystal growth and characterization of

- possible new magnetic topological insulators FeBi₂Te₄, J. Supercond. Nov. Magn. **33**, 2251 (2020).
- [22] P. E. Blöchl, Projector augmented-wave method, Phys. Rev. B 50, 17953 (1994).
- [23] G. Kresse and J. Hafner, Ab initio molecular-dynamics simulation of the liquid-metal-amorphous-semiconductor transition in germanium, Phys. Rev. B 49, 14251 (1994).
- [24] G. Kresse and J. Furthmüller, Efficient iterative schemes for ab initio total-energy calculations using a plane-wave basis set, Phys. Rev. B 54, 11169 (1996).
- [25] G. Kresse and D. Joubert, From ultrasoft pseudopotentials to the projector augmented-wave method, Phys. Rev. B 59, 1758 (1999).
- [26] J. P. Perdew, K. Burke, and M. Ernzerhof, Generalized gradient approximation made simple, Phys. Rev. Lett. 77, 3865 (1996).
- [27] A. I. Liechtenstein, V. I. Anisimov, and J. Zaanen, Density-functional theory and strong interactions: Orbital ordering in Mott-Hubbard insulators, Phys. Rev. B 52, R5467 (1995).
- [28] C. Hu, K. N. Gordon, P. Liu, J. Liu, X. Zhou, P. Hao, D. Narayan, E. Emmanouilidou, H. Sun, Y. Liu, H. Brawer, A. P. Ramirez, L. Ding, H. Cao, Q. Liu, D. Dessau, and N. Ni, A van der Waals antiferromagnetic topological insulator with weak interlayer magnetic coupling, Nat. Commun. 11, 97 (2020).
- [29] S. Grimme, Semiempirical GGA-type density functional constructed with a long-range dispersion correction, J. Comput. Chem. 27, 1787 (2006).
- [30] H. J. Monkhorst and J. D. Pack, Special points for Brillouin-zone integrations, Phys. Rev. B 13, 5188 (1976).
- [31] H. T. Stokes and D. M. Hatch, FINDSYM: program for identifying the space-group symmetry of a crystal, J. Appl. Cryst. 38, 237 (2005).
- [32] A. Togo and I. Tanaka, SpgLib: a software library for crystal symmetry search (2018), arXiv:1808.01590.
- [33] Y. Hinuma, G. Pizzi, Y. Kumagai, F. Oba, and I. Tanaka, Band structure diagram paths based on crystallography, Comput. Mater. Sci. 128, 140 (2017).
- [34] K. Parlinski, Z. Q. Li, and Y. Kawazoe, First-principles determination of the soft mode in cubic ZrO₂, Phys. Rev. Lett. 78, 4063 (1997).
- [35] T. Tadano, Y. Gohda, and S. Tsuneyuki, Anharmonic force constants extracted from first-principles molecular dynamics: applications to heat transfer simulations, J. Phys.: Condens. Matter 26, 225402 (2014).
- [36] K. Parlinski, Phonon, Cracow (2019).
- [37] Z. S. Aliev, I. R. Amiraslanov, D. I. Nasonova, A. V. Shevelkov, N. A. Abdullayev, Z. A. Jahangirli, E. N. Orujlu, M. M. Otrokov, N. T. Mamedov, M. B. Babanly, and E. V. Chulkov, Novel ternary layered manganese bismuth tellurides of the MnTe-Bi₂Te₃ system: Synthesis and crystal structure, J. Alloys Compd. 789, 443 (2019).
- [38] Y. Han, S. Sun, S. Qi, X. Xu, and Z. Qiao, Interlayer ferromagnetism and high-temperature quantum anomalous Hall effect in p-doped MnBi₂Te₄ multilayers, Phys. Rev. B 103, 245403 (2021).
- [39] R. Loudon, The raman effect in crystals, Adv. Phys. 50, 813 (2001).
- [40] Y. Cho, J. H. Kang, L. Liang, X. Kong, S. Ghosh, F. Kargar, C. Hu, A. A. Balandin, A. A. Puretzky, N. Ni, and C. W. Wong, Phonon modes and raman signatures of $MnBi_2nTe_{3n+1}$ (n=1,2,3,4) magnetic topological het-

- erostructures (2021), arXiv:2107.03204.
- [41] M. Rodriguez-Vega, A. Leonardo, and G. A. Fiete, Group theory study of the vibrational modes and magnetic order in the topological antiferromagnet MnBi₂Te₄, Phys. Rev. B 102, 104102 (2020).
- [42] C. Pei, Y. Xia, J. Wu, Y. Zhao, L. Gao, T. Ying, B. Gao, N. Li, W. Yang, D. Zhang, H. Gou, Y. Chen, H. Hosono, G. Li, and Y. Qi, Pressure-induced topological and structural phase transitions in an antiferromagnetic topological insulator, Chinese Phys. Lett. 37, 066401 (2020).
- [43] P. Mal, G. Bera, G. R. Turpu, S. K. Srivastava, A. Gangan, B. Chakraborty, B. Das, and P. Das, Vibrational spectra of Pb₂Bi₂Te₃, PbBi₂Te₄, and PbBi₄Te₇ topological insulators: temperature-dependent Raman and theoretical insights from DFT simulations, Phys. Chem. Chem. Phys. 21, 15030 (2019).
- [44] N. K. Singh, D. Rawat, D. Dey, A. Elsukova, P. O. A. Persson, P. Eklund, A. Taraphder, and A. Soni, Electronphonon coupling and quantum correction to topological magnetoconductivity in Bi₂GeTe₄, Phys. Rev. B 105, 045134 (2022).
- [45] J. Choe, D. Lujan, M. Rodriguez-Vega, Z. Ye, A. Leonardo, J. Quan, T. N. Nunley, L.-J. Chang, S.-F. Lee, J. Yan, G. A. Fiete, R. He, and X. Li, Electron– phonon and spin–lattice coupling in atomically thin layers of MnBi₂Te₄, Nano Lett. 21, 6139 (2021).
- [46] W. Richter and C. R. Becker, A raman and far-infrared investigation of phonons in the rhombohedral V_2 - VI_3 compounds Bi_2Te_3 , Bi_2Se_3 , Sb_2Te_3 and $Bi_2(Te_{1-x}Se_x)_3$ (0 < x < 1), ($Bi_{1-y}Sb_y)_2Te_3$ (0 < y < 1), Phys. Status Solidi B 84, 619 (1977).
- [47] V. Chis, I. Y. Sklyadneva, K. A. Kokh, V. A. Volodin, O. E. Tereshchenko, and E. V. Chulkov, Vibrations in binary and ternary topological insulators: Firstprinciples calculations and Raman spectroscopy measurements, Phys. Rev. B 86, 174304 (2012).
- [48] L. Goncalves, C. Couto, P. Alpuim, A. Rolo, F. Völklein, and J. Correia, Optimization of thermoelectric properties

- on bi2te3 thin films deposited by thermal co-evaporation, Thin Solid Films **518**, 2816 (2010).
- [49] K. M. F. Shahil, M. Z. Hossain, D. Teweldebrhan, and A. A. Balandin, Crystal symmetry breaking in fewquintuple Bi₂Te₃ films: Applications in nanometrology of topological insulators, Appl. Phys. Lett. 96, 153103 (2010).
- [50] B.-T. Wang and P. Zhang, Phonon spectrum and bonding properties of Bi₂Se₃: Role of strong spin-orbit interaction, Appl. Phys. Lett. 100, 082109 (2012).
- [51] J. O. Jenkins, J. A. Rayne, and R. W. Ure, Elastic moduli and phonon properties of Bi₂Te₃, Phys. Rev. B 5, 3171 (1972).
- [52] L. Zhang and Q. Niu, Angular momentum of phonons and the Einstein-de Haas effect, Phys. Rev. Lett. 112, 085503 (2014).
- [53] Y. Liu, C.-S. Lian, Y. Li, Y. Xu, and W. Duan, Pseudospins and topological effects of phonons in a kekulé lattice, Phys. Rev. Lett. 119, 255901 (2017).
- [54] L. Zhang and Q. Niu, Chiral phonons at high-symmetry points in monolayer hexagonal lattices, Phys. Rev. Lett. 115, 115502 (2015).
- [55] H. Chen, W. Wu, S. A. Yang, X. Li, and L. Zhang, Chiral phonons in kagome lattices, Phys. Rev. B 100, 094303 (2019).
- [56] A. Ptok, A. Kobiałka, M. Sternik, J. Lażewski, P. T. Jochym, A. M. Oleś, S. Stankov, and P. Piekarz, Chiral phonons in the honeycomb sublattice of layered CoSnlike compounds, Phys. Rev. B 104, 054305 (2021).
- [57] S. Coh, Classification of materials with phonon angular momentum and microscopic origin of angular momentum (2019), arXiv:1911.05064.
- [58] H. Chen, W. Zhang, Q. Niu, and L. Zhang, Chiral phonons in two-dimensional materials, 2D Mater. 6, 012002 (2018).
- [59] K. Momma and F. Izumi, VESTA3 for three-dimensional visualization of crystal, volumetric and morphology data, J. Appl. Crystallogr. 44, 1272 (2011).